



Comparison of the accuracy of analytical models for basalt fiber–reinforced poly(lactic acid) composites prepared by injection molding and fused filament fabrication

Csenge Tóth¹ · Norbert Krisztián Kovács^{1,2}

Received: 26 January 2022 / Accepted: 17 June 2022 / Published online: 30 June 2022
© The Author(s) 2022

Abstract

We compared the accuracy of analytical models for short fiber–reinforced composites prepared by injection molding and fused filament fabrication (FFF). The microstructural features define the strength of the composites, and they are greatly dependent on the processing conditions. We collected data on fiber length, orientation, and porosity via X-ray micro-computed tomography (μ -CT) and determined the critical fiber length experimentally. We used this data as input for the modified rule of mixtures and the modeling framework based on the Halpin–Tsai method, and found that the cumulative error for FFF is more than twice that for injection-molded composites. We also showed that experimentally determined matrix strength for FFF gives a lower strength limit which is applicable for engineering parts. We presented a new approach for the modeling of the tensile strength of neat FFF products, in which the printed structure is divided into contact zones and bulk material zones. The matrix strength calculated this way was found to approximate the experimental results with an error of 5%.

Keywords Analytical modeling · Composite · Fused filament fabrication · Injection molding

1 Introduction

The demand for high-performance, recyclable structural components has promoted the development of thermoplastic composite technologies. Thermoplastic polymers offer the advantages of recyclability, easy joining methods [1], and the possibility to produce multi-functional and smart materials [2], and short fibers are often used as reinforcement to improve their strength and stiffness [3, 4]. In most cases, short fiber–reinforced composites (SFCs) are processed by injection molding (IM). Although IM seems unbeatable in productivity, it is not economical for custom production. Thus, fused filament fabrication (FFF) is emerging as a new potential.

The mechanical properties of SFCs are strongly dependent on their microstructure [5–8]. Fiber length distribution (FLD), fiber orientation distribution, and potential voids are all affected by the processing conditions; therefore, they are expected to differ for different technologies. Regarding orientation, IM composites have a sandwich-like morphology with fibers aligned parallel to the flow direction in the shell, and randomly oriented fibers in the core [9]. FFF composites, on the other hand, are highly oriented along the printing direction. The fiber length distribution is usually wide for IM and FFF as well, due to the fiber breakage caused by shear forces during melt processing. Lastly, the void content for IM is zero or negligible, while in FFF parts, it is significant [10–14].

Quantitative data on these microstructural features can be used to refine predictive models for SFCs.

There are several methods for the micromechanical modeling of IM composites.

Chin et al. [15] reported that statistical distribution functions can be used to describe FLD, and the ratio of the length-weighted and the numerical average length (the index of distribution) can be used for elastic modulus prediction. Hine et al. [16] investigated the effect of FLD numerically, and they found that the distribution function can be replaced

✉ Norbert Krisztián Kovács
kovacsnp@pt.bme.hu

¹ Department of Polymer Engineering, Faculty of Mechanical Engineering, Budapest University of Technology and Economics, Műegyetem rkp. 3., H-1111 Budapest, Hungary

² MTA-BME Lendület Lightweight Polymer Composites Research Group, Műegyetem rkp. 3., H-1111 Budapest, Hungary

by the numerical average length. Mortazavian and Fatemi [17] fitted a three-parameter probability density function to the fiber length and used it to modify the linear rule of mixtures for tensile strength prediction. Fiber orientation density was also taken into account. For elastic moduli prediction, they compared several analytical models and found that models that include the orientation distribution are more accurate. Lionetto et al. [18] described FLD with the two-parameter Weibull probability density function, then they used the mean value of fiber length in the modified Halpin–Tsai equation to calculate elastic moduli.

Being a younger technology, the micromechanical modeling of FFF composites is less discussed in literature yet. van de Werken et al. [4] used the distribution functions for length and orientation to refine the Halpin–Tsai model and the laminate analogy approach. They reported good agreement between the predicted and the experimental tensile strength and modulus. Somireddy et al. [19] applied the classical lamination theory (CLT) and the Tsai–Hill failure criteria, and they found that the voids degrade mechanical properties and reduce the accuracy of predictive methods. Papon et al. [20] identified three types of voids and considered their effects in a multi-level analytical modeling framework. They found that the void distribution can be obtained from stochastic void models, and it can be used with the CLT to give accurate predictions for the overall laminate properties. Besides the microstructural features, the fiber content is also important. Nasirov et al. [21] investigated short fiber–reinforced composites with a fiber content of up to 10 v% and they reported that the Mori–Tanaka homogenization method is very effective for higher fiber contents. However, their findings suggest that there might be differences in using homogenization models for composites with different fiber contents.

Micromechanical models are widely used for SFCs, and the goodness of the predictions can be refined by taking microstructural features into account. There are several metrics for describing fiber length and orientation, but which one gives more accurate results is less discussed. It is also known that different melt processing technologies create different microstructures in the products. However, differences in the applicability and the accuracy of the models are also rarely addressed in the literature.

In this study, we aim to compare the accuracy of the modified rule of mixtures (MROM) for SFCs prepared by IM and FFF. For this purpose, we prepared basalt fiber–reinforced poly(lactic acid) filaments and granules with 5, 10, and 20 wt% fiber contents. We presented the microstructural differences between the technologies via X-ray micro-computed tomography, during which data on fiber length, orientation, and void content was collected. We used three different metrics to describe the fiber length and showed which gives the most accurate estimate for tensile strength. Lastly, we

proposed a new approach for the mechanical modeling of products made with FFF technology.

2 Experimental procedure

2.1 Materials

The matrix of the composites was poly(lactic acid) (PLA, Ingeo 3100 HP, Natureworks LLC, USA). Its density is 1.24 g/cm³ and its D-lactide content is approx. 0.5% [22].

Short basalt fibers were obtained from Kamenny Vek with an initial fiber length and diameter of 10 mm and 12 μm, respectively. The density of basalt fibers is 2.59 g/cm³. The fibers were cut from continuous yarn. The fibers are surface-treated with silane by the manufacturer, which can provide good adhesion with thermoplastic matrix materials [23–25]. To avoid possible hydrolytic degradation, we dried the raw materials at 80 °C for 4 h prior to processing. Further material parameters used for the shrinkage simulation can be seen in Table 1.

2.2 Sample preparation

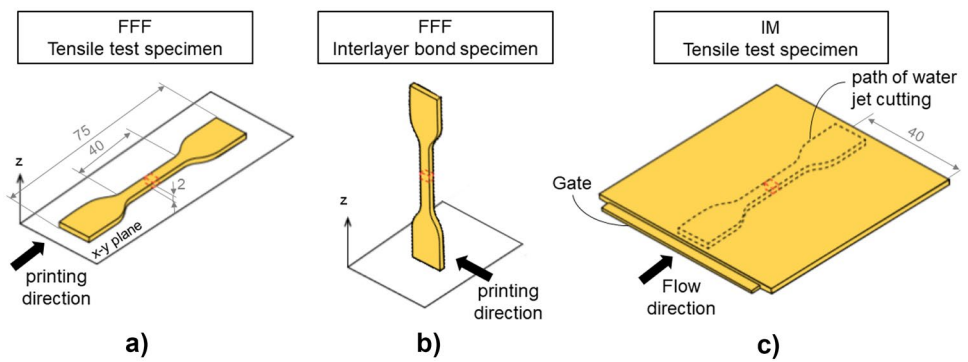
Composite compounds were prepared with a LabTech Scientific co-rotating twin-screw extruder (screw diameter = 26 mm, L/D = 44) with a temperature profile of 170–175–180–185–190 °C (from the hopper to the die) and a screw speed of 25 rpm. Dry mixtures with fiber contents of 5, 10, and 20 wt% were fed to the extruder, then the compounds were pelletized and extruded again for homogeneous fiber distribution. For filament fabrication, the compounds were extruded through a cylindrical die and the diameter required (1.75 mm) was controlled by draw speed.

To investigate the differences between processing technologies, we prepared injection-molded and 3D-printed specimens as well. Samples for tensile testing (based on type 5B, ISO 527–1:2012 as can be seen in Fig. 1a) were produced on a Craftbot + type desktop FFF printer. We printed the samples with a nozzle temperature of 230 °C, a layer height of 0.2 mm, and an infill rate of 100%, with the printing orientation parallel to the longitudinal axis (0°). We also

Table 1 Material parameters used for the shrinkage simulation [22, 26–29]

Material parameter	Poly(lactic acid)	Basalt fiber
Linear coefficient of thermal expansion (°C ⁻¹)	7.7e-5	3.6e-6
Storage/Young's modulus (MPa)	E(T)	80,000
Poisson's ratio	0.3	0.2

Fig. 1 Tensile specimen geometries. **a** FFF printed with flat printing orientation, **b** FFF printed with standing orientation, and **c** injection-molded specimens



prepared neat PLA samples with a standing printing orientation (Fig. 1b) to determine interlayer bond strength.

80 × 80 × 2 mm plates were injection molded with an Arburg Allrounder Advance 270S 400–170 (ARBURG GmbH, Lossburg) injection molding machine, with a melt temperature of 190 °C and a mold temperature of 25 °C, an injection rate of 50 cm³/s, and a holding pressure of 600 bar. The tensile specimen was cut by water jet cutting from the center of the parts with the longitudinal axis of the samples parallel to the flow direction (Fig. 1c).

2.3 Tensile testing

We conducted tensile tests to experimentally validate the analytical methods presented with a Zwick Z005 (Zwick Roell AG, Ulm) universal testing machine in accordance with the ISO 527–1:2012 standard, with a cross-head speed of 5 mm/min, and a gripping distance of 50 mm, at 25 °C and in 20% relative humidity. We tested 5 specimens for each sample type.

2.4 Interfacial shear strength measurements

The adhesion between the fibers and the matrix has a great influence on the mechanical properties of the composites. One way to quantify adhesion is to measure the interfacial shear strength with microdroplet pullout tests [30]. For this purpose, we took single basalt fibers out of the continuous yard and fixed them onto paper frames for easier handling. Then, we placed a single drop of PLA melt on the fibers (as shown in Fig. 2a) using a soldering iron. The dimensions required to determine the strength (the embedded length (*L*) and fiber diameter (*d*)) were measured with an Olympus optical microscope. We placed the samples in a custom grip and performed the pull-out tests using a Zwick Z005 (Zwick Roell AG, Ulm) universal testing machine at a testing speed of 2 mm/min. Figure 2b, c shows a specimen and the experimental arrangement. We repeated the experiment on at least 20 samples.

The interfacial adhesion is affected by pressure, which can differ by orders of magnitude between IM and FFF. To check if the test is representative of both technologies,

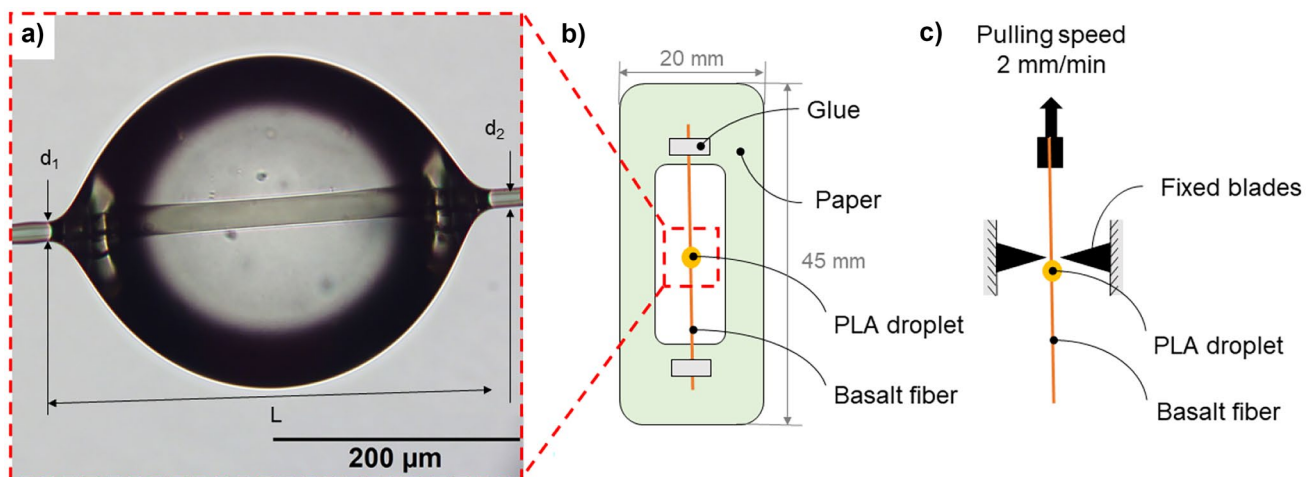


Fig. 2 **a** Micrograph of a PLA drop on basalt fiber and its relevant parameters (*L* (mm) is the embedded length, *d*₁ and *d*₂ (mm) are the fiber diameters); **b** schematic diagram of a test specimen; **c** experimental arrangement

we prepared a shrinkage simulation using Ansys R3 2019. A single fiber of 14- μm diameter and a 100- μm diameter polymer cylinder were modeled with overlap at the contact surface. Material parameters used as input can be seen in Table 1. We assumed isotropic material behavior for simplicity, and creep was not considered. We calculated shrinkage from an initial temperature of 200 $^{\circ}\text{C}$ with a 10 $^{\circ}\text{C}/\text{min}$ cooling rate which represents the conditions of sample preparation. The simulation showed that the pressure on the fiber surface is of the same magnitude as the pressure in the injection mold, with a maximum value of 263.5 MPa at 20 $^{\circ}\text{C}$. Therefore, we expect no difference in the development of fiber-matrix adhesion as a function of processing technology.

Using the interfacial shear strength results, we determined the critical fiber length with the Kelly-Tyson equation (Eq. (1)) [31].

$$l_{\text{crit}} = \frac{\sigma_f d_f}{2\tau} \quad (1)$$

where l_{crit} (mm) is the critical fiber length, τ (MPa) is the interfacial shear strength of the fiber-matrix interface, σ_f (MPa) is the ultimate tensile strength of a single fiber, and d_f (mm) is the fiber diameter.

2.5 Microstructural analysis

We performed micro-computed tomography with a GE Phoenix Micromex 180 PCB (Baker Hughes Company, Houston) X-ray device to examine and quantify the internal morphological features of the composites. 4 \times 2 \times 5 mm samples were cut from the middle of the specimens and rotated 360 $^{\circ}$ while being exposed to an X-ray beam (accelerating voltage: 180 kV; power: 20 W). We collected the images and reconstructed the 3D geometry with the Volume Graphics Studio Max software. After correcting image artifacts, a 5 \times 3 \times 1.6 mm region of interest was defined, which reduced the amount of data to be processed. Phases in the composites were segmented with gray level values based on the density differences of the materials (Fig. 3). Void content was determined by summing the volumes corresponding to gray levels of 6000 and below. We also determined the fiber orientation tensor components using fiber composite material analysis.

For the fiber length distribution analysis, we approximated the fiber lengths with the major axis of the inscribed ellipse. Based on the data, we calculated the averages of fiber length (Eq. (2)), the length-weighted averages (Eq. (3)), and the fiber length distribution functions (Eq. (4)) as well [32].

$$L_n = \frac{\sum n_i L_i}{\sum n_i} \quad (2)$$

Fig. 3 Regions of interest for X-ray μ -CT analysis in the case of (a) FFF and (b) IM composites. The matrix, the fibers and the voids in the composites are segmented according to their density differences and colored with gray, orange and blue, respectively

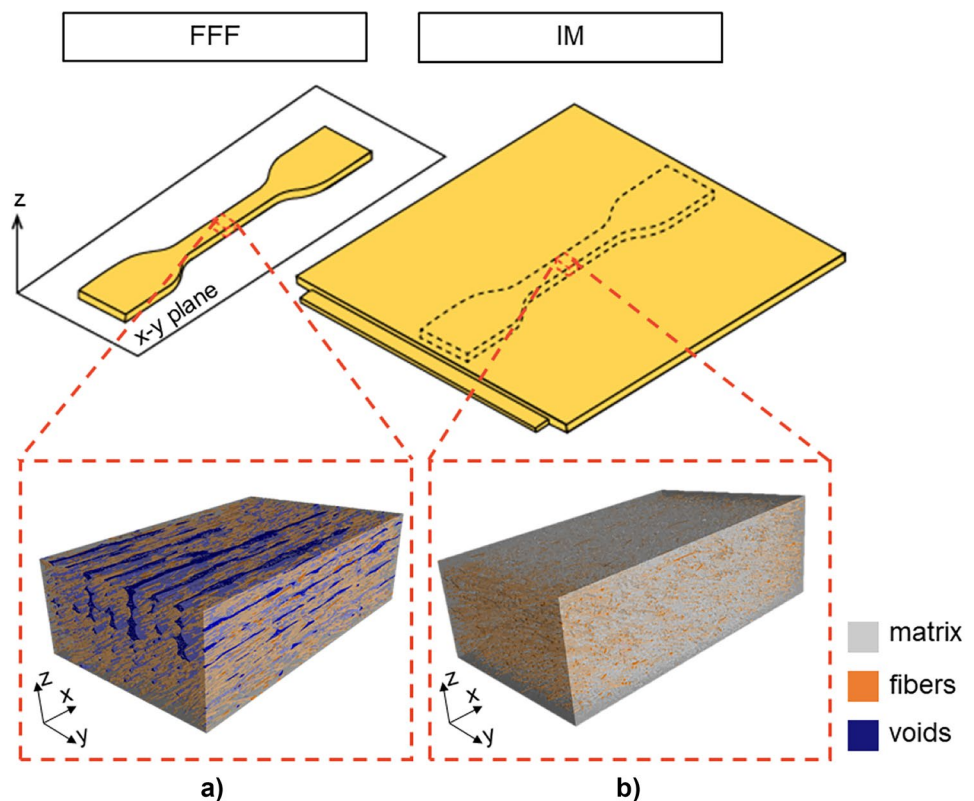


Table 2 Input data used to calculate the critical fiber length, and the result

Interfacial shear strength τ (MPa)	Tensile strength of a single fiber σ_f (MPa)	Fiber diameter d_f (μm)	Critical fiber length l_{crit} (mm)
12.0 ± 3.5	2335.3 ± 360.1	13.2 ± 1.4	1.4 ± 0.5

$$L_w = \frac{\sum n_i L_i^2}{\sum n_i L_i} \tag{3}$$

where L_i (μm) is the length of fiber i and n_i is the number of fibers of length L_i .

$$f(l) = \frac{N_i/N}{\Delta l} \tag{4}$$

where N is the total number of the fibers within all intervals, N_i is the i th interval, and Δl is the fiber length interval.

Scanning electron microscopy (SEM) was also used for further inspection and validation of the data collected with μ -CT analysis. Images of cryogenic fracture surfaces were acquired with a JEOL JSM 6380LA (JEOL Ltd., Tokyo) scanning electron microscope. The samples were coated with a thin layer of gold to prevent charging by the electron beam. Lastly, in order to determine the dimensions of the cross-sections, we used a Keyence VHX-5000 (Keyence Corporation, Mechelen) digital microscope with $\times 20$ magnification and the ImageJ software.

3 Results and discussion

3.1 Fiber length distribution and critical fiber length

We determined the fiber length distribution after injection molding and 3D printing of the samples for each fiber content, and also calculated critical fiber length (Table 2). The fiber length distributions of the FFF-printed and the injection-molded composites are shown in Fig. 4, and the averages are presented in Table 3.

There was a large reduction in fiber length compared to the initial length of 10 mm during compounding, then further fiber breakage occurred during processing. The numerical averages and the weighted averages are all below the critical fiber length, so no increase in tensile strength can be expected. For FFF, these fiber length results are in line with the literature. Most data reported for fiber length is in the range of 50–300 microns [6, 14, 21, 33], with a maximum fiber length achieved in one instance being 480 microns [12]. In the case of injection molding, residual fiber length can be orders of magnitude longer with long-fiber granules [34, 35] or direct fiber feeding [36], but in this study, we aimed for uniform processing conditions to ensure comparability.

3.2 Fiber orientation

The performance of short-fiber composites greatly depends on the orientation distribution in the part. The orientation

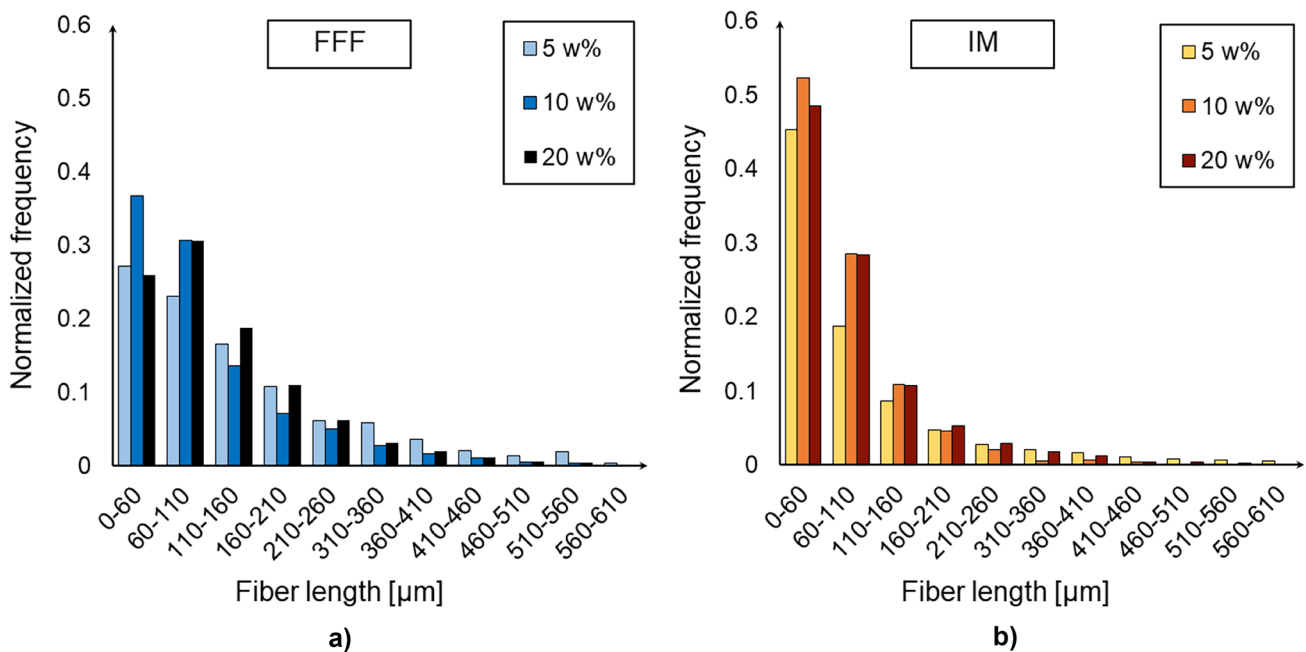


Fig. 4 Fiber length distributions of the 5, 10, and 20 wt% composites prepared by **a** FFF and **b** injection molding

Table 3 Numerical and length-weighted fiber length averages and standard deviations

Process	Fiber content v_f (wt%)	Numerical average L_n (μm)	Length-weighted average L_w (μm)
FFF	5	103.4 ± 106.4	216.4 ± 494.5
	10	81.4 ± 89.1	311.4 ± 262.7
	20	145.1 ± 84.6	195.3 ± 607.1
Injection molding	5	112.4 ± 115.7	224.8 ± 104.3
	10	101.7 ± 90.2	140.3 ± 529.7
	20	111.1 ± 77.4	163.6 ± 293.9

of the short fibers can vary from random to unidirectional depending on the processing conditions, so we compared the orientation of the 3D printed and the injection-molded samples based on the μ -CT analysis. To characterize the distribution, the fiber orientation tensor (Eq. (5)) is often used, where the diagonal elements are between 0 and 1 (1 indicating perfect alignment) [37].

$$A_{ij} = \begin{bmatrix} a_{xx} & a_{xy} & a_{xz} \\ a_{yx} & a_{yy} & a_{yz} \\ a_{zx} & a_{zy} & a_{zz} \end{bmatrix} \quad (5)$$

For visual representation, we plotted the principal diagonal values (a_{xx} , a_{yy} , a_{zz}) of the second-order orientation tensor as a function of edge length (Fig. 5), thus describing orientation along the whole inspected region.

The results show that in the case of 3D printing, the fibers are highly oriented in the printing direction, and the distribution does not seem to be affected by fiber content. For the injection-molded samples, the orientation vector along the x -axis was similar to that of the y -axis, which means that fibers are equally likely to be oriented parallel to and perpendicular to the injection direction. As the fiber content

increases from 5 to 10 wt%, orientation also increases as the core–shell structure becomes more prominent.

3.3 Porosity

In addition to fiber length and orientation, the quality of composites is greatly affected by their void content. Using data obtained by μ -CT, we segmented and quantified the voids according to their volume (Fig. 6). There is no sign of porosity in the injection-molded samples, although the micro-voids that can occur at the fiber ends can only be detected up to the limit of the resolution of the X-ray microscope (6.5 μm).

In the case of FFF samples, we observed smaller, uniformly distributed voids near the print bed and larger pores along the building direction. This may be due to the damping effect of the polymer layers. Near the print bed, higher pressure can be provided during extrusion thus creating a more compact structure. However, as the number of layers increases, damping can also increase but the applied pressure remains constant. We also observed that the voids between the printed filaments decreased with increasing fiber content, which is in agreement with the literature [6, 12].

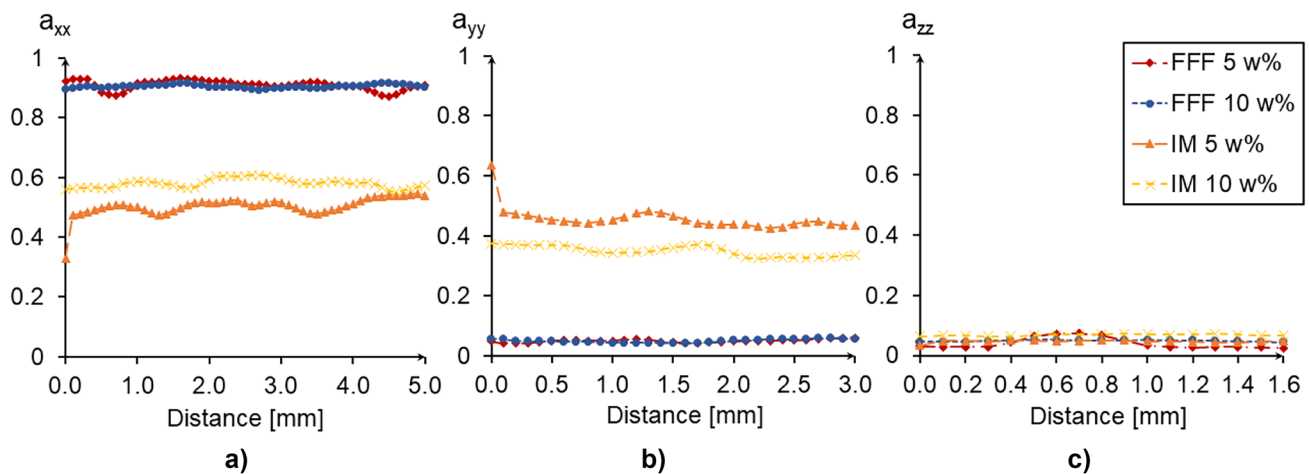


Fig. 5 Fiber orientation distribution of FFF-printed and injection-molded composites with 5 and 10 wt% fiber content. The principal diagonal values of the second-order orientation tensor (a_{xx} , a_{yy} , a_{zz}) are shown as a function of edge length (distance)

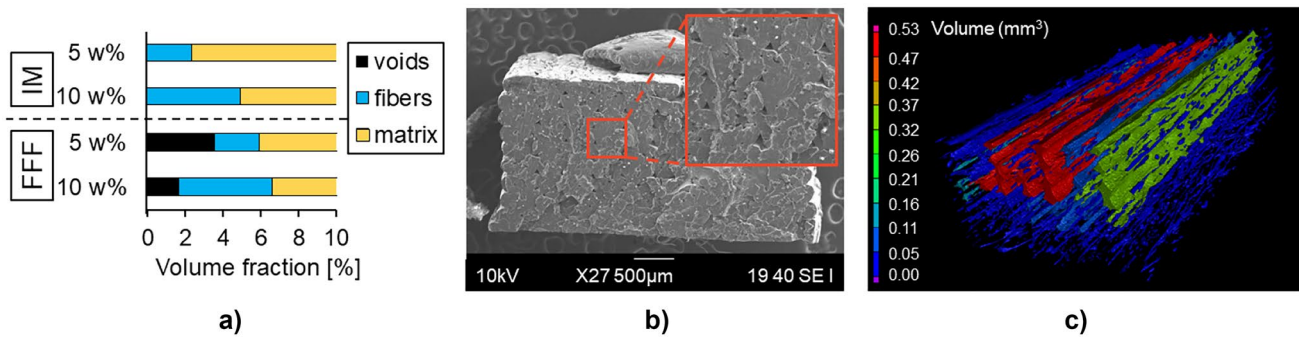


Fig. 6 Porosity of FFF-printed and injection-molded composites with 5 and 10 wt% fiber content. **a** The volume fraction of voids, fibers, and matrix phases; **b** the SEM micrograph of the fracture surface of

the FFF 5 wt% sample and **c** the size distribution of voids in the FFF 5 wt% sample

3.4 Analytical modeling and experimental testing of tensile strength

The presented microstructural features (fiber length and orientation) can serve as input parameters for various analytical models to predict the mechanical properties of the composites. Since the average fiber lengths (L_n, L_w) are below the critical length for all the samples, the fiber length factor (χ_1) can be determined with Eq. (6). In this case, uniform fiber length is assumed. We calculated the length correction factor using the arithmetic and the length-weighted fiber length averages as well [31].

$$\chi_1 = \frac{L}{2L_{crit}} \text{ for } L < l_{crit} \quad (6)$$

where L (mm) is the average fiber length and L_{crit} (mm) is the critical fiber length.

For samples with non-uniform fiber length, first we have to determine the fiber length distribution function. Then, the fiber length factor is modified according to Eq. (7). The second term is zero in this case, since the number of fibers exceeding the critical fiber length is zero for each sample.

$$\chi_1 = \int_{L_{min}}^{L_{crit}} \left[\frac{l^2}{2L_{crit}L_{mean}} \right] f(l) dl + \int_{L_{crit}}^{L_{max}} \left(\frac{l}{L_{mean}} \right) \left[1 - \frac{L_{crit}}{2l} \right] f(l) dl \quad (7)$$

where L_{mean} (mm) is the mean fiber length; L_{crit} (mm) is the critical fiber length; L_{min} and L_{max} (mm) are the shortest and the longest fibers measured, respectively; and $f(l)$ is the fiber length distribution function.

After the fiber length factor is calculated based on all three approaches, the MROM (Eq. (8)) can be used for the prediction of tensile strength. We made calculations with all three factors (χ_1 based on L_n and L_w and determined with the fiber length distribution) in order to determine which gives a more accurate estimate.

$$\sigma_{MROM} = \chi_1 \sigma_f v_f + \sigma_m v_m \quad (8)$$

where χ_1 (–) is the fiber length factor; σ_f (MPa) and σ_m (MPa) are the ultimate tensile strength of a fiber and the matrix, respectively; and v_f (–) and v_m (–) are the fiber and the matrix volume fractions, respectively.

Theoretically, a more accurate prediction can be achieved if we take into account fiber orientation as well. van de Werken et al. [4] reported a modeling framework based on the Halpin–Tsai equation (Eq. (9)), which includes the orientation factor (χ_2). In this paper, the orientation factor is approximated by the principal diagonal value of the second-order orientation tensor in the direction of stress. For unidirectional composites, $\chi_2 = 1$.

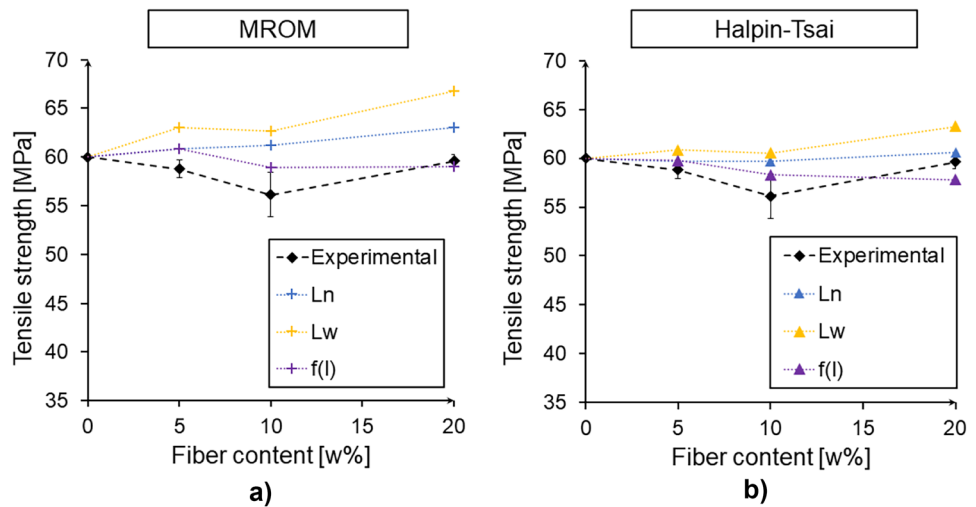
$$\sigma_{HT} = \chi_1 \chi_2 \sigma_f v_f + \sigma_m v_m \quad (9)$$

where χ_1 (–) is the fiber length factor; χ_2 (–) is the orientation factor; σ_f (MPa) and σ_m (MPa) are the ultimate tensile strength of a fiber and the matrix, respectively; and v_f (–) and v_m (–) are the fiber and the matrix volume fractions, respectively.

The calculated and the experimental tensile strengths for IM and FFF composites are shown in Fig. 7. We also plotted the residuals (the error between the predicted values and the experimental data) to compare the accuracy of the different models (Fig. 8a, b), then we plotted the sum of the absolute values of the residuals in increasing order (Fig. 8c). For FFF composites, Fig. 9 shows the calculated and the experimental tensile strengths, and the residuals can be seen in Fig. 10.

In the case of injection molding, all methods besides MROM L_w give good prediction with a 5% deviation. Length-weighted average reduces accuracy, while the FLD function $f(l)$ approximates the experimental results the best. The orientation factor further refines the estimate, and if it is used, the FLD function can be replaced by the numerical average length, which simplifies the

Fig. 7 Predicted tensile strengths based on the **a** MROM and **b** the Halpin–Tsai model, and experimental results for IM composites



calculations. These results underline that fiber orientation in IM composites influences mechanical properties strongly; therefore, it should not be neglected in analytical modeling.

For 3D printing, the application of the methods is not straightforward in terms of interpreting the strength of the neat matrix. Injection-molded PLA has a tensile strength of 60 MPa, while the strength measured on 3D printed samples only reaches 43.7 MPa. This raises the following question: which value for matrix strength gives a more accurate estimate for the composites? We made predictions using both and showed that approximations using the strength of the IM matrix overestimate and the neat FFF strength underestimates the experimental results. For neat PLA, the loss in strength is due to the voids, so calculations with the experimental matrix strength include their effect. Calculation with FFF strength defines a lower limit that can be applied safely for engineering parts.

Regarding the correction factors, it can be seen that similar to IM, the FLD function gives the best estimate; however, the numerical average closely follows. This means that $f(l)$ can also be replaced with L_n for FFF calculations.

Orientation, however, does not seem to have a significant effect on the accuracy of the model since fiber orientation in the extruded filaments is nearly unidirectional. The orientation, therefore, should not be corrected; rather, laminate mechanics can be used to take advantage of the unidirectional nature of the layers.

The difference between the accuracy of the models shows that application for 3D printed composites might require a different approach. In the FFF process, the material is deposited layer-by-layer, and molecular diffusion between layers is often incomplete. Thus, interlayer bonding strength does not reach the strength of the bulk material [38], which causes anisotropy in the strength of the 3D printed structure. Therefore, models that assume homogeneous strength for the matrix material may be inaccurate.

If the bond strength between the layers is below the strength within the filament, we can divide FFF printed parts into bulk material zones and contact zones (as shown in Fig. 11). Knowing the layer height and the number of layers, the size of the contact zones can be approximated based on optical microscopic images (Fig. 12). We defined the width of the contact zone as the minimum width of the

Fig. 8 Residual plots for IM. **a** Halpin–Tsai and **b** MROM, **c** the sum of the residuals in increasing order

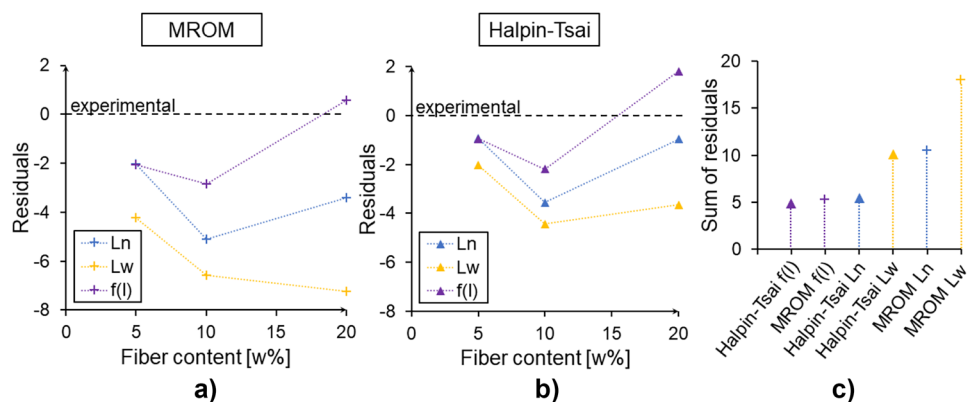
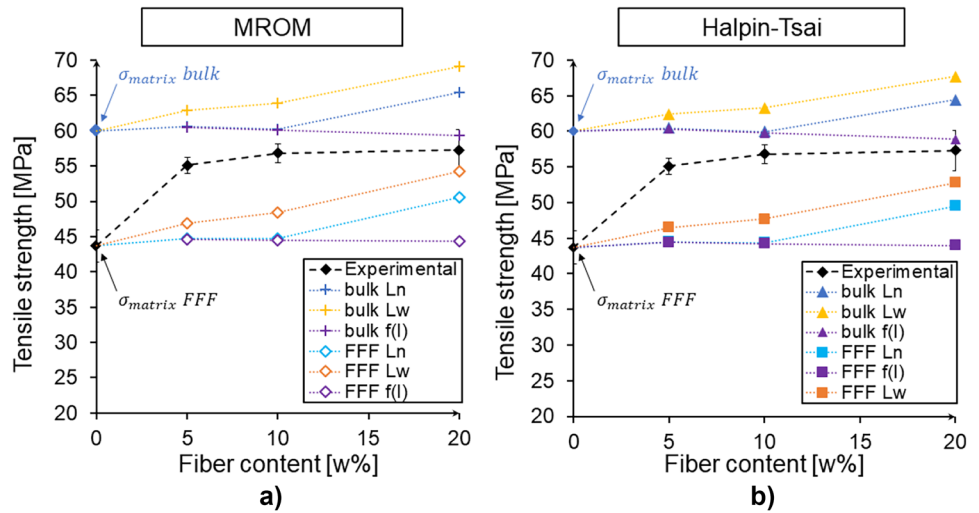


Fig. 9 Predicted tensile strengths based on the **a** MROM and **b** the Halpin–Tsai model, and experimental results for FFF composites



cross-section, and the height was approximated by the height of the intersection of ellipses representing the elementary filaments. The volume fraction of all contact areas can be determined by Eq. (10).

$$v_c = \frac{(n - 1)(W_b H_b L)}{v_{all}} \tag{10}$$

where n is the number of layers, L (mm) is the length, v_{all} (mm³) is the volume of the specimen, W_b (mm) is the length, and H_b (mm) is the height of the interlayer contact.

The volume of the specimen is given by Eq. (11).

$$v_{all} = W_{sample} \cdot H_{sample} \cdot L \tag{11}$$

Then we can calculate the strength of the matrix material based on the Rule of Mixtures (Eq. (12)) [39]. The tensile strength of the bulk material zones was assumed to be equal to injection-molded strength, and the bonding strength of the contact zones was determined experimentally (12.5 ± 5 MPa).

$$\sigma_{mROM} = \sigma_{bulk}(1 - v_c) + \sigma_z v_c \tag{12}$$

where σ_{bulk} (MPa) and σ_z (MPa) are the strength of the bulk material and the strength of the contact zones, respectively, and v_c (–) is the volume fraction of the contact zones.

Tensile strength calculated this way considers the anisotropy of the matrix material of 3D printed structures. We entered the new matrix strength into the presented predictive models as shown in Eqs. (13) and (14). Matrix strength

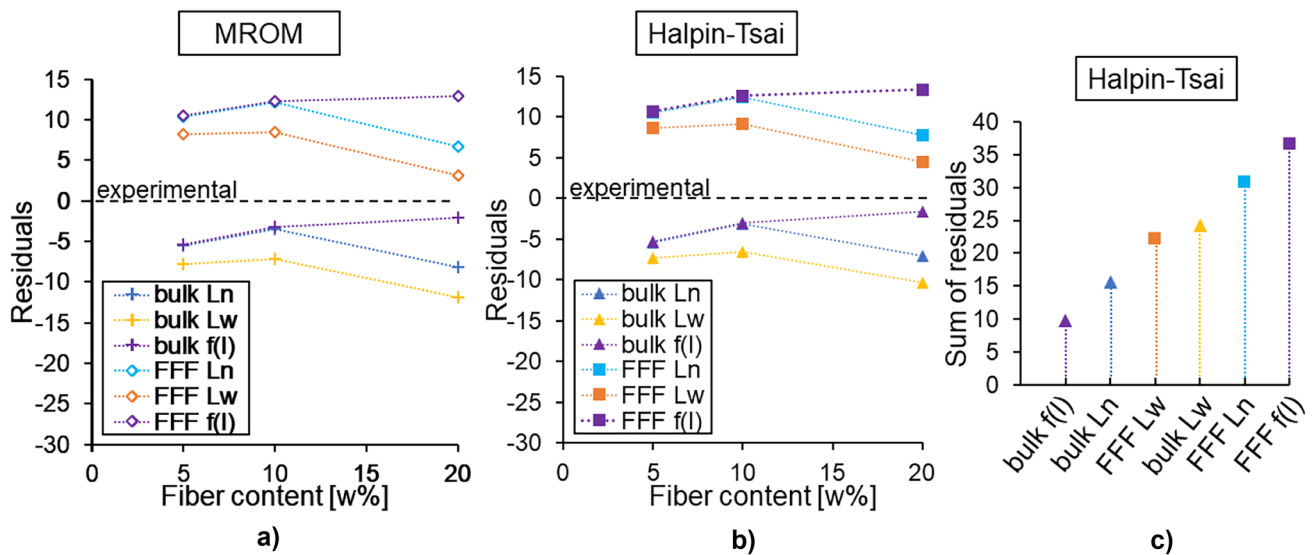


Fig. 10 Residual plots for FFF. **a** Halpin–Tsai and **b** MROM, **c** the sum of the residuals in increasing order

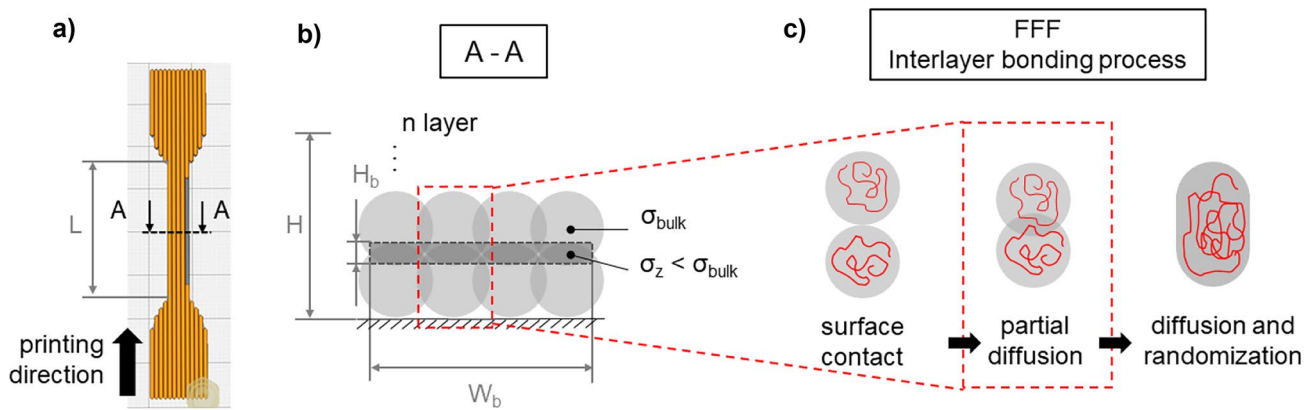
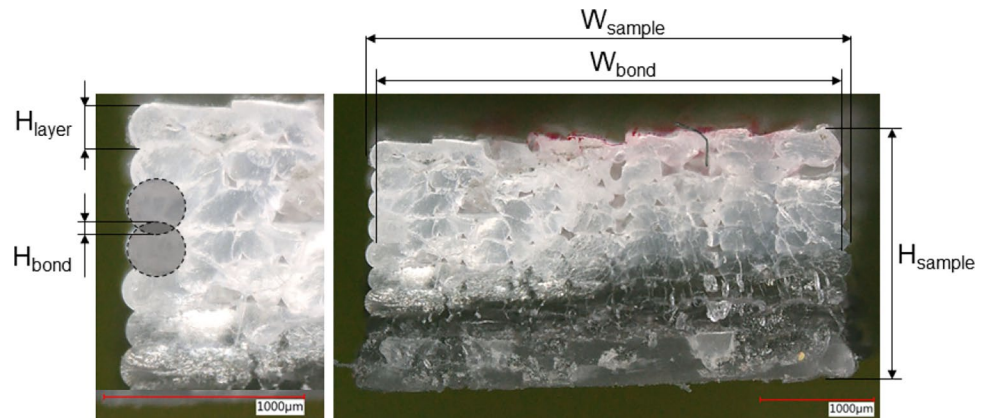


Fig. 11 Definition of contact zones. **(a)** Tested area of the tensile specimen; **(b)** interpretation of different strength zones in the cross-section; **(c)** general state of molecular diffusion between layers

Fig. 12 Definition of contact zones via optical microscopy



calculated with the ROM approximates the experimental values with an error of 5%, which suggests that the approach is appropriate for predicting the tensile strength of neat FFF parts. For composites, the accuracy of the analytical methods varies as a function of fiber content. This can be because as fiber content increases, more fibers are present in the contact area, thus changing interlayer strength. Further refinements should also cover the theoretical definition of interlayer strength and the size of the contact zones.

$$\sigma_{\text{MROMnew}} = \chi_1 \sigma_f v_f + (1 - v_f) \sigma_{\text{mROM}} \quad (13)$$

$$\sigma_{\text{HTnew}} = \chi_1 \chi_2 \sigma_f v_f + (1 - v_f) \sigma_{\text{mROM}} \quad (14)$$

where χ_1 (–) is the fiber length factor; χ_2 (–) is the orientation factor; σ_f (MPa) is the ultimate tensile strength of a fiber; v_f (–) and v_m (–) are the fiber and the matrix volume fractions, respectively; and σ_{mROM} (MPa) is the matrix strength calculated with the rule of mixtures.

4 Conclusion

In this study, we compared the applicability of homogenization models for strength prediction of short fiber-reinforced composites prepared by injection molding (IM) and fused filament fabrication (FFF). We investigated basalt fiber-reinforced PLA composites with 5, 10, and 20 wt% fiber contents. We determined fiber length distribution, fiber orientation, and porosity via X-ray μ -CT, then we used this data for the analytical prediction of the tensile strength based on the modified rule of mixtures (MROM) and the Halpin–Tsai model. We found that in the case of IM, correction with the orientation factor gives the most accurate predictions. For FFF, the orientation factor is not significant due to the nearly unidirectional fiber arrangement in the layers. The FLD function can be replaced with the numerical length average for both technologies, which simplifies the calculations.

It was also shown that in the case of FFF, inserting the experimental matrix strength into models results in a lower tensile strength limit as the effect of voids is already considered. When designing load-bearing parts, the lower limit of strength is estimated for safety; therefore, calculations with the experimental tensile strength can provide good and useful results.

We also presented a new approach for refining predictive methods for FFF composites. As the bond strength between the layers is below the strength of the bulk material, the 3D printed structure can be segmented into bulk material zones and contact zones. Based on the rule of mixtures, we calculated tensile strength and found that the resulting value approximates the strength of the neat PLA with an error of 5%. Our findings provide a more precise approach for the modeling of FFF composites, thus contributing to industrial applicability. In our future studies, we aim to investigate the effect of fiber content on interlayer bond strength, and we also aim to further refine the model with theoretical calculations of bond strength.

Acknowledgements We would like to express our gratitude to Elas Kft. for the access to X-ray microtomography measurements.

Author contribution Each author participated sufficiently in the work. C. T. produced the samples and conducted the mechanical tests and data analysis. N. K. generated the funding for the work and provided lab resources. All authors contributed to and reviewed the final manuscript.

Funding Open access funding provided by Budapest University of Technology and Economics. This work was supported by the National Research, Development and Innovation Office, Hungary (2018–1.3.1-VKE-2018–00001, OTKA FK134336 and OTKA K 138472) and by the Italian-Hungarian bilateral agreement (grant number NKM-73/2019) of the Hungarian Academy of Sciences. The research reported in this paper and carried out at BME has been supported by the NRDI Fund (TKP2020 NC, Grant No. BME-NCS) based on the charter of bolster issued by the NRDI Office under the auspices of the Ministry for Innovation and Technology.

Data availability Data presented in the paper is available from the corresponding author on reasonable request.

Declarations

Competing interests The authors declare no competing interests.

Open Access This article is licensed under a Creative Commons Attribution 4.0 International License, which permits use, sharing, adaptation, distribution and reproduction in any medium or format, as long as you give appropriate credit to the original author(s) and the source, provide a link to the Creative Commons licence, and indicate if changes were made. The images or other third party material in this article are included in the article's Creative Commons licence, unless indicated otherwise in a credit line to the material. If material is not included in the article's Creative Commons licence and your intended use is not permitted by statutory regulation or exceeds the permitted use, you will need to obtain permission directly from the copyright holder. To view a copy of this licence, visit <http://creativecommons.org/licenses/by/4.0/>.

References

1. Takács L, Szabó F (2020) Experimental and numerical failure analysis of adhesive joint of glass fiber reinforced polymer composite. *Period Polytech Mech Eng* 64:88–95. <https://doi.org/10.3311/PPme.15106>
2. Sikhosana ST, Gumede TP, Malebo NJ, Ogundeji AO (2021) Poly(Lactic acid) and its composites as functional materials for 3-d scaffolds in biomedical applications: a mini-review of recent trends. *Express Polym Lett* 15:568–580. <https://doi.org/10.3144/expresspolymlett.2021.48>
3. Akintayo OS, Olajide JL, Betiku OT et al (2020) Poly(Lactic acid)-silkworm silk fibre/fibroin bio-composites: a review of their processing, properties, and nascent applications. *Express Polym Lett* 14:924–951. <https://doi.org/10.3144/expresspolymlett.2020.76>
4. van de Werken N, Tekinalp H, Khanbolouki P et al (2020) Additively manufactured carbon fiber-reinforced composites: state of the art and perspective. *Addit Manuf* 31:100962. <https://doi.org/10.1016/j.addma.2019.100962>
5. Yu S, Hwang JY, Hong SH (2020) 3D microstructural characterization and mechanical properties determination of short basalt fiber-reinforced polyamide 6,6 composites. *Compos Part B Eng* 187:107839. <https://doi.org/10.1016/j.compositesb.2020.107839>
6. Yu S, Hwang YH, Hwang JY, Hong SH (2019) Analytical study on the 3D-printed structure and mechanical properties of basalt fiber-reinforced PLA composites using X-ray microscopy. *Compos Sci Technol* 175:18–27. <https://doi.org/10.1016/j.compscitech.2019.03.005>
7. Zhong Y, Liu P, Pei Q et al (2020) Elastic properties of injection molded short glass fiber reinforced thermoplastic composites. *Compos Struct* 254:112850. <https://doi.org/10.1016/j.compstruct.2020.112850>
8. Wu K, Wan L, Zhang H, Yang D (2018) Numerical simulation of the injection molding process of short fiber composites by an integrated particle approach. *Int J Adv Manuf Technol* 97:3479–3491. <https://doi.org/10.1007/s00170-018-2204-6>
9. Tseng HC, Chang RY, Hsu CH (2020) Comparison of recent fiber orientation models in injection molding simulation of fiber-reinforced composites. *J Thermoplast Compos Mater* 33:35–52. <https://doi.org/10.1177/0892705718804599>
10. Ferreira RTL, Amatte IC, Dutra TA, Bürger D (2017) Experimental characterization and micrography of 3D printed PLA and PLA reinforced with short carbon fibers. *Compos Part B Eng* 124:88–100. <https://doi.org/10.1016/j.compositesb.2017.05.013>
11. Gonabadi H, Chen Y, Yadav A, Bull S (2022) Investigation of the effect of raster angle, build orientation, and infill density on the elastic response of 3D printed parts using finite element microstructural modeling and homogenization techniques. *Int J Adv Manuf Technol* 118:1485–1510. <https://doi.org/10.1007/s00170-021-07940-4>
12. Tekinalp HL, Kunc V, Velez-Garcia GM et al (2014) Highly oriented carbon fiber-polymer composites via additive manufacturing. *Compos Sci Technol* 105:144–150. <https://doi.org/10.1016/j.compscitech.2014.10.009>
13. Hanon MM, Marcziš R, Zsidai L (2021) Influence of the 3D printing process settings on tensile strength of PLA and HT-PLA. *Period Polytech Mech Eng* 65:38–46. <https://doi.org/10.3311/PPme.13683>
14. Hofstätter T, Gutmann IW, Koch T et al (2016) Distribution and orientation of carbon fibers in polylactic acid parts produced by fused deposition modeling. *Proc - ASPE/euspen 2016 Summer Top Meet Dimens Accuracy Surf Finish Addit Manuf* 44–49

15. Chin W-K, Liu H-T, Lee Y-D (1988) Effects of fiber length and orientation distribution on the elastic modulus of short fiber reinforced thermoplastics. *Polym Compos* 9:27–35. <https://doi.org/10.1002/pc.750090105>
16. Hine PJ, Rudolf H, Gusev AA (2002) Numerical simulation of the effects of volume fraction, aspect ratio and fibre length distribution on the elastic and thermoelastic properties of short fibre composites. 62:1445–1453
17. Mortazavian S, Fatemi A (2015) Composites : part B effects of fiber orientation and anisotropy on tensile strength and elastic modulus of short fiber reinforced polymer composites 72:116–129. <https://doi.org/10.1016/j.compositesb.2014.11.041>
18. Lionetto F, Montagna F, Natali D et al (2021) Correlation between elastic properties and morphology in short fiber composites by X-ray computed micro-tomography. *Compos Part A* 140:106169. <https://doi.org/10.1016/j.compositesa.2020.106169>
19. Somireddy M, Singh CV, Czekanski A (2020) Mechanical behaviour of 3D printed composite parts with short carbon fiber reinforcements. *Eng Fail Anal* 107:104232. <https://doi.org/10.1016/j.engfailanal.2019.104232>
20. Papon EA, Haque A, Mulani SB (2019) Process optimization and stochastic modeling of void contents and mechanical properties in additively manufactured composites. *Compos Part B Eng* 177:107325. <https://doi.org/10.1016/j.compositesb.2019.107325>
21. Nasirov A, Gupta A, Hasanov S, Fidan I (2020) Three-scale asymptotic homogenization of short fiber reinforced additively manufactured polymer composites. *Compos Part B Eng* 202:108269. <https://doi.org/10.1016/j.compositesb.2020.108269>
22. Tábi T (2019) The application of the synergistic effect between the crystal structure of poly(lactic acid) (PLA) and the presence of ethylene vinyl acetate copolymer (EVA) to produce highly ductile PLA/EVA blends. *J Therm Anal Calorim* 138:1287–1297
23. Kurniawan D, Kim BS, Lee HY, Lim JY (2015) Towards improving mechanical properties of basalt fiber/poly(lactic acid) composites by fiber surface treatments. *Compos Interfaces* 22:553–562. <https://doi.org/10.1080/09276440.2015.1054743>
24. Liu S, Wu G, Yu J et al (2019) Surface modification of basalt fiber (BF) for improving compatibilities between BF and poly(lactic acid) (PLA) matrix. *Compos Interfaces* 26:275–290. <https://doi.org/10.1080/09276440.2018.1499353>
25. Deák T, Czigány T, Tamás P, Németh C (2010) Enhancement of interfacial properties of basalt fiber reinforced nylon 6 matrix composites with silane coupling agents. *Express Polym Lett* 4:590–598. <https://doi.org/10.3144/expresspolymlett.2010.74>
26. Kuciel S, Mazur K, Marek H (2020) The influence of wood and basalt fibres on mechanical, thermal and hydrothermal properties of PLA composites. *J Polym Environ*. <https://doi.org/10.1007/s10924-020-01677-z>
27. Sarasini F, Tirillò J, Seghini MC (2018) Influence of thermal conditioning on tensile behaviour of single basalt fibres. *Compos Part B Eng* 132:77–86
28. Ferreira R, Amatte I, Assis D, Bürger D (2017) Experimental characterization and micrography of 3D printed PLA and PLA reinforced with short carbon fibers. *Compos Part B Eng*. <https://doi.org/10.1016/j.compositesb.2017.05.013>
29. Yu S, Bale H, Park S, Hwang JY, Hong SH (2021) Anisotropic microstructure dependent mechanical behavior of 3D-printed basalt fiber-reinforced thermoplastic composites. *Compos Part B Eng* 224:109184
30. Revol BP, Thomassey M, Ruch F et al (2017) Single fibre model composite: interfacial shear strength measurements between reactive polyamide-6 and cellulosic or glass fibres by microdroplet pullout test. *Compos Sci Technol* 148:9–19. <https://doi.org/10.1016/j.compscitech.2017.05.018>
31. Fu S-Y, Lauke B, Mai Y-W (2009) 3 - Major factors affecting the performance of short fibre reinforced polymers. In: Fu S-Y, Lauke B, Mai Y-WBT-S and E of SFRPC (eds) *Woodhead Publishing Series in Composites Science and Engineering*. Woodhead Publishing, pp 29–58
32. Fu S-Y, Lauke B, Mai Y-W (2009) 5 - Strength of short fibre reinforced polymers. In: Fu S-Y, Lauke B, Mai Y-WBT-S and E of SFRPC (eds) *Woodhead Publishing Series in Composites Science and Engineering*. Woodhead Publishing, pp 80–118
33. Sang L, Han S, Li Z et al (2019) Development of short basalt fiber reinforced polylactide composites and their feasible evaluation for 3D printing applications. *Compos Part B Eng* 164:629–639. <https://doi.org/10.1016/j.compositesb.2019.01.085>
34. Tábi T, Égerházi AZ, Tamás P et al (2014) Investigation of injection moulded poly(lactic acid) reinforced with long basalt fibres. *Compos Part A Appl Sci Manuf* 64:99–106. <https://doi.org/10.1016/j.compositesa.2014.05.001>
35. Tábi T, Tamás P, Kovács JG (2013) Chopped basalt fibres: a new perspective in reinforcing poly(lactic acid) to produce injection moulded engineering composites from renewable and natural resources. *Express Polym Lett* 7:107–119. <https://doi.org/10.3144/expresspolymlett.2013.11>
36. Yan X, Cao S (2018) Structure and interfacial shear strength of polypropylene-glass fiber/carbon fiber hybrid composites fabricated by direct fiber feeding injection molding. *Compos Struct* 185:362–372. <https://doi.org/10.1016/j.compstruct.2017.11.037>
37. Advani SG, Tucker CL (2016) The use of tensors to describe and predict fiber orientation in short fiber composites University of Illinois at Urbana-Champaign, 1206 West Green. *J Rheol (N Y N Y)* 751
38. Coogan TJ, Kazmer DO (2020) Prediction of interlayer strength in material extrusion additive manufacturing. *Addit Manuf* 35:101368. <https://doi.org/10.1016/j.addma.2020.101368>
39. Bartolai J, Simpson TW, Xie R (2016) Predicting strength of thermoplastic polymer parts produced using additive manufacturing. *Solid Free Fabr 2016 Proc 27th Annu Int Solid Free Fabr Symp - An Addit Manuf Conf SFF 2016* 951–963

Publisher's note Springer Nature remains neutral with regard to jurisdictional claims in published maps and institutional affiliations.